Contents

Chapter 3

Experiment, Results and Discussion

Contents

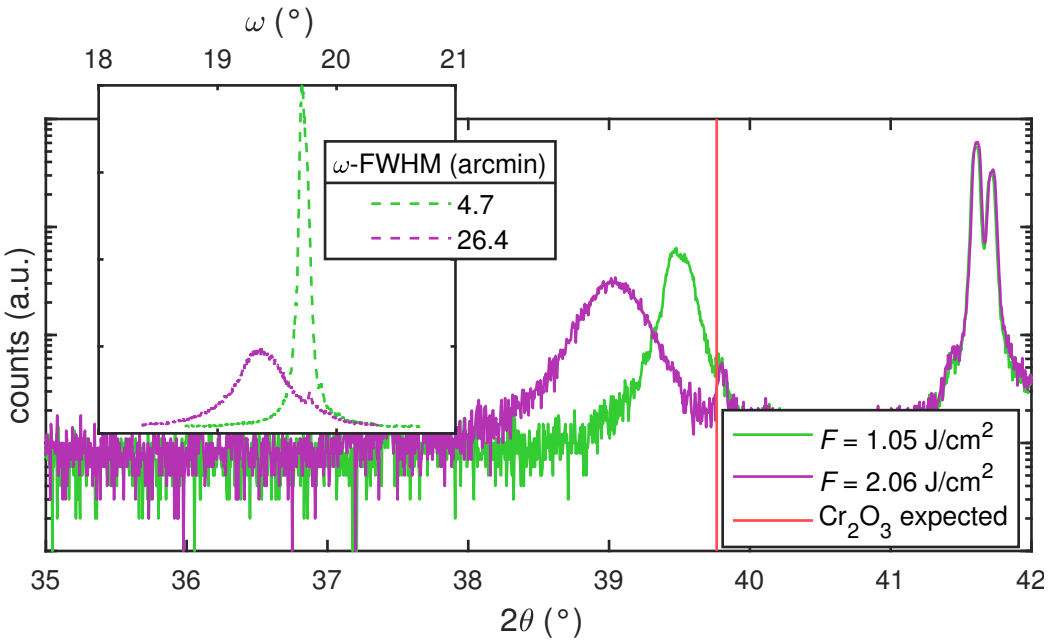

Figure 3.19: 2ϑ-ω-patterns for two *c*-plane samples fabricated with different laser focus on the target. The inset displays the diffractograms of the corresponding ω-scans performed on the respective reflections. The ZnO-doped (low) target was used without a fixed r_{PLD} but with uniform ablation on the whole target surface.

3.3 Strain Analysis

The structural properties of the thin film, namely its mosaicity and lattice distortion depend crucially on the growth process. It turned out that the absorption of energy at the laser entrance window alters the growth rate and the crystallinity much more dominantly than the growth temperature or the oxygen partial pressure (cf. 3.1). A similar effect was observed when targets were used for fabrication that exhibit a non-planar surface and tracks that were carved during previous ablations (cf. 3.2). Because the structural properties of the thin film also influence its electrical properties (cf. 3.2), the following investigations focus on the origin of the observed variations in strain and ω-FWHM. This is further motivated by the observation that a deliberate and controlled variation of laser spot size on the target surface yields a large reduction of ω-FWHM as well as a reduced shift of the peak position in the 2ϑ-ω-pattern (Fig. 3.19). This was achieved by varying the lens position (cf. 2.1) such that the laser spot size increases, yielding smaller fluence and larger ablation area on the target surface.

3.3.1 Experiment

Sample Fabrication

For all following depositions, the laser entrance window was cleaned before each process. A pure Cr_2O_3 target was used for deposition of thin films on $5 \times 5\,\mathrm{mm}^2$ sapphire substrates in the four aforementioned orientations. The first batch of samples was produced by only varying the pulse number to achieve a series of thin films with varying

thickness but constant laser fluence during deposition[9]. The pulse energy was set to 650 mJ and the lens position[10] to −2 cm, the resulting fluence is approx. 2 J cm^{-2}. This corresponds to the standard configuration during all previous processes (pink square in Fig. 2.2). This was repeated with fewer pulse number variations for three other lens positions, namely 0 cm, 1 cm and 2 cm, resulting in lower fluences: In Fig. 2.2, the yellow circles represent the probed laser fluences. This set of samples is referred to as the 1st batch.

To investigate the influence of fluence independent of ablation area, a 2nd batch of samples was fabricated with a fixed lens position (−1 cm) but varying laser pulse energy: 300 mJ, 450 mJ, 650 mJ and 800 mJ. The pulse number was adjusted to achieve approximately same thicknesses. The achieved fluences are visualized as red triangles in Fig. 2.2.

Measurements

For all samples, 2ϑ-ω-scans as well as ω-scans were performed. The reflections probed by the latter were (00.6), (02.4), (30.0) and (22.0) for *c*-, *r*-, *m*- and *a*-plane, respectively. For some selected samples of different thickness and fluence from the 1st batch, transmission measurements have been performed. The thickness of all samples was determined by spectroscopic ellipsometry measurements. To obtain more information about the relation between in-plane and out-of-plane lattice constants, Reciprocal Space Maps (RSMs) were performed on selected samples:

***c*-plane** For *c*-plane samples, the thickness series of the 1st batch that was fabricated with the largest laser spot size (lowest fluence) was investigated. The asymmetric reflection that was used for probing the relaxation process is (02.10), which has an inclination angle of approx. 32° with respect to the sample surface.

***r*-plane** All *r*-plane samples fabricated in the 2nd batch with different laser pulse energies were investigated. For each sample, the *x*-axis of the sample – containing the projection of the *c*-axis – is found by performing a φ-scan on the (03.0) reflection: This set of lattice planes has an inclination with respect to the surface, so the position of the peak in the diffraction pattern of the φ-scan reveals the *x*-axis. In this azimuth, an RSM is recorded around the asymmetric (03.0) reflection and the symmetric (02.4) reflection. By rotating $\Delta\phi = 90°$, the *y*-axis lays in the scattering plane and another RSM is performed around the symmetric (02.4) reflection. The twofold measurement of the symmetric reflection is necessary to calculate a possible lattice plane tilt for both *x*- and *y*-direction. Note that no shear is calculated due to the asymmetric nature of the (03.0) reflection with respect to the *r*-orientation[11]. After performing the various

[9] The series of thicknesses that was achieved in the prior experiments was correlated to a series of growth rates.

[10] Note that the values for the lens position have an arbitrary offset; a value of 0 cm does not correspond to the position where the target surface is in focus.

[11] For *m*- and *a*-plane rhombohedral structures, the crystal is symmetric under the transformation $\phi \to \phi + 180°$, which is not the case for *r*-plane.

corrections described in 2.2.4, the tilt angles can be calculated for both azimuths by

$$\theta = \arccos\left(\frac{q_\perp}{|\mathbf{q}|}\right) \cdot \operatorname{sgn}\left(q_\parallel\right) , \tag{3.4}$$

with $q_\perp$ and $q_\parallel$ being the out-of-plane (o.o.p.) and in-plane (i.p.) components of the scattering vector $\mathbf{q}$, respectively. The i.p. and o.o.p. strains are determined by comparing the observed scattering vector to the expected scattering vector for the (03.0) reflection:

$$\mathbf{q}_{(03.0)} = \left|\mathbf{q}_{(03.0)}\right| \cdot \begin{pmatrix} \cos\alpha_{(03.0)|r} \\ \sin\alpha_{(03.0)|r} \end{pmatrix} , \tag{3.5}$$

with $|\mathbf{q}_{(03.0)}|$ calculated from Equ. 2.6 and Equ. 2.7. $\alpha_{(03.0)|r}$ denotes the angle between the (03.0) reflection and the normal of the r-planes; it can be calculated from Equ. 2.8:

$$\alpha_{(03.0)|r} = 90° - \left(\alpha_{(03.0)|c} - \alpha_{(01.2)|c}\right) = \alpha_{(01.2)|c} = 57.62° . \tag{3.6}$$

***m*-plane** Similar to above, all m-plane samples from the 2nd batch were investigated. The samples were aligned to the x-axis by performing a φ-scan on the asymmetric (30.6) reflection, and an RSM was recorded afterwards. By rotating $\Delta\phi = 180°$ while maintaining 2θ and ω, the scattering condition for $(30.\overline{6})$ is probed and an RSM was recorded. The symmetric reflection (30.0) was also measured in this azimuth. The tilt angle and shear angle can be calculated according to Equ. 3.4 and Equ. 2.13, respectively. The lattice constants can be calculated from the components of the scattering vectors:

$$a_\perp = \frac{\sqrt{12}}{q_\perp^{(30.\pm6)}} , \tag{3.7}$$

$$a_\perp = \frac{\sqrt{12}}{q_\perp^{(03.0)}} , \tag{3.8}$$

$$c = \frac{6}{q_\parallel^{(30.\pm6)}} . \tag{3.9}$$

$a_\perp$ denotes the a lattice constant in direction of the normal to the sample surface. By rotating $\Delta\phi = 90°$, the y-axis can be probed via asymmetric reflections $(\overline{4}2.0)$ and (22.0), which differ in the azimuth by $\Delta\phi = 180°$. A second symmetric reflection (30.0) is recorded in this azimuth. Similar to the x-axis, the tilt and shear angles, as well as the lattice constants can be calculated:

$$(4\overline{2}.0): \quad a_\perp = \frac{\sqrt{12}}{q_\perp^{(4\overline{2}.0)}} \quad , \quad a_\parallel = \frac{2}{q_\parallel^{(4\overline{2}.0)}} , \tag{3.10}$$

$$(22.0): \quad a_\perp = \frac{\sqrt{12}}{q_\perp^{(22.0)}} \quad , \quad a_\parallel = \frac{2}{q_\parallel^{(22.0)}} , \tag{3.11}$$

$$(30.0): \quad a_\perp = \frac{\sqrt{12}}{q_\perp^{(03.0)}} . \tag{3.12}$$

$a_\parallel$ denotes the a lattice constant parallel to the y-axis. For detailed calculations of the former equations, see A.1. Note that all 6 measured reflections yield a value for $a_\perp$, and 2 measured reflections each yield 2 values for c and $a_\parallel$, respectively. Therefore, for each lattice constant, the mean value is evaluated and the error is estimated by the standard deviation.

***a*-plane** All a-plane samples from the 2nd batch were investigated and the method is similar to the one applied to the m-plane samples. The azimuth of the x-axis is found by performing a φ-scan on the (22.6) reflection, which also served for an RSM. Rotating by $\Delta\phi = 180°$ yields the $(22.\overline{6})$ reflection and (22.0) is also measured. Similar to above, the sample is rotated by 90° to align to the y-axis and two more asymmetric reflections are recorded: (30.0) and (03.0). A second RSM of (22.0) is also performed. This yields the following lattice constants for the x-axis:

$$a_\perp = \frac{4}{q_\perp^{(22.\pm6)}}\,, \tag{3.13}$$

$$a_\perp = \frac{4}{q_\perp^{(22.0)}}\,, \tag{3.14}$$

$$c = \frac{6}{q_\parallel^{(22.\pm6)}}\,, \tag{3.15}$$

and for the y-axis:

$$(30.0): \quad a_\perp = \frac{2}{q_\perp^{(30.0)}} \cdot \frac{3}{2} \quad , \quad a_\parallel = \frac{2}{\sqrt{3} q_\parallel^{(30.0)}} \cdot \frac{3}{2}\,, \tag{3.16}$$

$$(03.0): \quad a_\perp = \frac{2}{q_\perp^{(03.0)}} \cdot \frac{3}{2} \quad , \quad a_\parallel = \frac{2}{\sqrt{3} q_\parallel^{(03.0)}} \cdot \frac{3}{2}\,, \tag{3.17}$$

$$(22.0): \quad a_\perp = \frac{4}{q_\perp^{(22.0)}}\,. \tag{3.18}$$

For detailed calculations and the origin of the factor $\frac{3}{2}$, see A.2. Again, lattice constants obtained from several reflections, the mean and standard deviation are calculated.

3.3.2 Results

The analysis of the data will not be structured into the 1st and 2nd batch, but into the analysis of (i) c-plane, (ii) r-plane and (iii) m- and a-plane samples. In the following, some general remarks on the fabricated samples will be made.

In Fig. 3.20, a detailed view into the growth rates of the samples of the 1st batch is given. First of all, for a fixed fluence (fixed lens position), increasing the pulse number decreases the growth rate. This is expected, because the coating of the laser entrance window increases during the process. By fixing a pulse number, an increase in growth rate is observed for a regime of decreasing fluence from 2 to 1 $\mathrm{J\,cm^{-2}}$ (Fig 3.20 bottom). This can be explained by the fact that the reduction of fluence is due to increasing laser spot size. When the fluence is still above the ablation threshold for the target material, an increasing ablation area results in an increasing growth rate. But at some point the fluence is too low ablate the material and then the growth rate decreases, even though the ablation area increases. This can be observed at around 1.2 $\mathrm{J\,cm^{-2}}$ in Fig. 3.20, which is therefore an estimate for the ablation threshold.

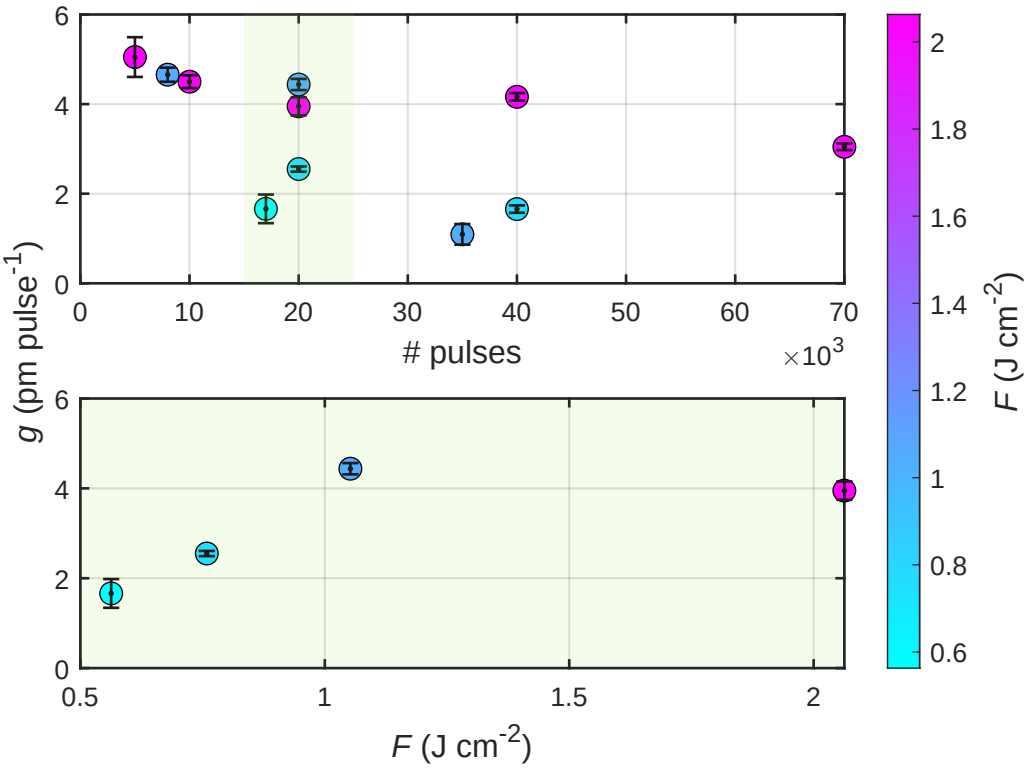

Figure 3.20: Growth rates of the samples from the 1st batch, depending on the pulse number (top) and depending on the laser fluence on the target for an approx. fixed pulse number (bottom). The data points are the mean of the four samples with another orientation each, that were obtained from every process. The errorbar displays the standard deviation.

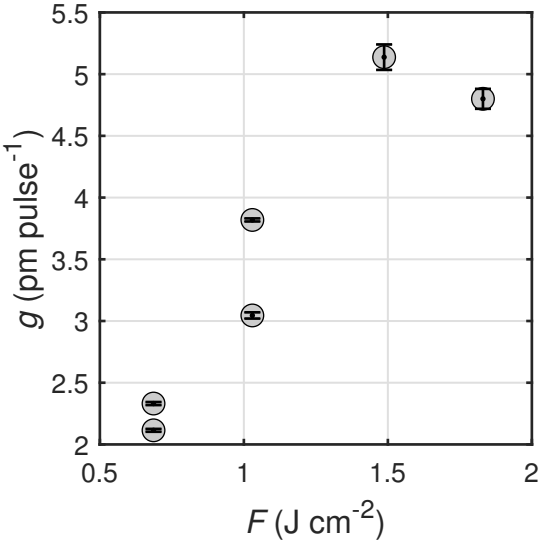

Figure 3.21: Growth rates of samples from the 2nd batch, depending on laser fluence on the target surface. The data points are the mean of thicknesses of the four orientations, similar to Fig. 3.20.

Bibliography

[1] Neil W. Ashcroft and N. David Mermin. *Solid State Physics*. Saunders College Publishing, 1976. 826 pp.

[2] George F. Harrington and José Santiso. "Back-to-Basics tutorial: X-ray diffraction of thin films". In: *Journal of Electroceramics* 47.4 (2021), pp. 141–163. ISSN: 1385-3449, 1573-8663. DOI: 10.1007/s10832-021-00263-6.

[3] Lothar Spieß, ed. *Moderne Röntgenbeugung: Röntgendiffraktometrie für Materialwissenschaftler, Physiker und Chemiker*. 2., überarb. und erw. Aufl. Studium. Wiesbaden: Vieweg + Teubner, 2009. 564 pp. ISBN: 978-3-8351-0166-1.

[4] Aoife B Kehoe et al. "Assessing the potential of Mg-doped Cr_2O_3 as a novel p-type transparent conducting oxide". In: *Journal of Physics: Condensed Matter* 28.12 (2016), p. 125501. ISSN: 0953-8984, 1361-648X. DOI: 10.1088/0953-8984/28/12/125501.

[5] David S. Ginley, ed. *Handbook of Transparent Conductors*. Boston, MA: Springer US, 2011. ISBN: 978-1-4419-1637-2 978-1-4419-1638-9. DOI: 10.1007/978-1-4419-1638-9.

[6] Anna Hassa, Marius Grundmann, and Holger Von Wenckstern. "Progression of group-III sesquioxides: epitaxy, solubility and desorption". In: *Journal of Physics D: Applied Physics* 54.22 (2021), p. 223001. ISSN: 0022-3727, 1361-6463. DOI: 10.1088/1361-6463/abd4a4.

[7] Clemens Petersen et al. "PLD of α-Ga_2O_3 on m-plane Al_2O_3: Growth regime, growth process, and structural properties". In: *APL Materials* 11.6 (2023), p. 061122. ISSN: 2166-532X. DOI: 10.1063/5.0149797.

[8] S.I. Stepanov et al. "HVPE growth of corundum-structured α-Ga2O3 on sapphire substrates with α-Cr2O3 buffer layer". In: *Materials Physics and Mechanics* 47 (2021), pp. 577–581. DOI: 10.18149/MPM.4742021_4.

[9] N. Uekawa and K. Kaneko. "Dopant Reduction in p-Type Oxide Films upon Oxygen Absorption". In: *The Journal of Physical Chemistry* 100.10 (1996), pp. 4193–4198. ISSN: 0022-3654, 1541-5740. DOI: 10.1021/jp952784m.

[10] P. S. Robbert et al. "Novel electronic and magnetic properties of ultrathin chromium oxide films grown on Pt(111)". In: *Journal of Vacuum Science & Technology A: Vacuum, Surfaces, and Films* 16.3 (1998), pp. 990–995. ISSN: 0734-2101, 1520-8559. DOI: 10.1116/1.581283.

[11] M.F. Al-Kuhaili and S.M.A. Durrani. "Optical properties of chromium oxide thin films deposited by electron-beam evaporation". In: *Optical Materials* 29.6 (2007), pp. 709–713. ISSN: 09253467. DOI: 10.1016/j.optmat.2005.11.020.

[12] François Lebreau et al. “Structural, Magnetic, Electronic, Defect, and Diffusion Properties of Cr_2O_3: A DFT+U Study”. In: *The Journal of Physical Chemistry C* 118.31 (2014), pp. 18133–18145. ISSN: 1932-7447. DOI: 10.1021/jp5039943.

[13] Zhishan Mi et al. “The effects of strain and vacancy defects on the electronic structure of Cr_2O_3”. In: *Computational Materials Science* 144 (2018), pp. 64–69. ISSN: 09270256. DOI: 10.1016/j.commatsci.2017.12.012.

[14] Jarnail Singh et al. “Structural, optical and electrical characterization of epitaxial Cr_2O_3 thin film deposited by PLD”. In: *Materials Research Express* 6.10 (2019), p. 106406. ISSN: 2053-1591. DOI: 10.1088/2053-1591/ab3543.

[15] Chun-Shen Cheng, H. Gomi, and H. Sakata. “Electrical and Optical Properties of Cr_2O_3 Films Prepared by Chemical Vapour Deposition”. In: *Physica Status Solidi (a)* 155.2 (1996), pp. 417–425. ISSN: 00318965, 1521396X. DOI: 10.1002/pssa.2211550215.

[16] Cecilia Guillén and José Herrero. “Structural Changes Induced by Heating in Sputtered NiO and Cr_2O_3 Thin Films as p-Type Transparent Conductive Electrodes”. In: *Electronic Materials* 2.2 (2021), pp. 49–59. ISSN: 2673-3978. DOI: 10.3390/electronicmat2020005.

[17] M. Catti et al. “Electronic, magnetic and crystal structure of Cr_2O_3 by theoretical methods”. In: *Journal of Physics and Chemistry of Solids* 57.11 (1996), pp. 1735–1741. ISSN: 00223697. DOI: 10.1016/0022-3697(96)00034-0.

[18] Larry W. Finger and Robert M. Hazen. “Crystal structure and isothermal compression of Fe_2O_3, Cr_2O_3, and V_2O_3 to 50 kbars”. In: *Journal of Applied Physics* 51.10 (1980), pp. 5362–5367. ISSN: 0021-8979, 1089-7550. DOI: 10.1063/1.327451.

[19] Elisabetta Arca et al. “Effect of Chemical Precursors On the Optical and Electrical Properties of p-Type Transparent Conducting Cr_2O_3:(Mg,N)”. In: *The Journal of Physical Chemistry C* 117.42 (2013), pp. 21901–21907. ISSN: 1932-7447. DOI: 10.1021/jp404230k.

[20] Valerian Pishchik, Leonid A. Lytvynov, and Elena R. Dobrovinskaya. *Sapphire: Material, Manufacturing, Applications*. Boston, MA: Springer US, 2009. ISBN: 978-0-387-85694-0 978-0-387-85695-7. DOI: 10.1007/978-0-387-85695-7.

[21] M. Marezio and J. P. Remeika. “Bond lengths in the α-Ga_2O_3 structure and the high-pressure phase of $Ga_{2-x}Fe_xO_3$”. In: *The Journal of Chemical Physics* 46.5 (1967), pp. 1862–1865. ISSN: 0021-9606, 1089-7690. DOI: 10.1063/1.1840945.

[22] Ruihua Cheng, C.N. Borca, and P.A. Dowben. “Selective Area Chemical Vapor Deposition of Chromium Oxides”. In: *MRS Proceedings* 614 (2000), F10.4.1. ISSN: 0272-9172, 1946-4274. DOI: 10.1557/PROC-614-F10.4.1.

[23] Ruihua Cheng et al. “Characterization of the native Cr_2O_3 oxide surface of CrO_2”. In: *Applied Physics Letters* 79.19 (2001), pp. 3122–3124. ISSN: 0003-6951, 1077-3118. DOI: 10.1063/1.1416474.

[24] Ruihua Cheng et al. "Potential phase control of chromium oxide thin films prepared by laser-initiated organometallic chemical vapor deposition". In: *Applied Physics Letters* 78.4 (2001), pp. 521–523. ISSN: 0003-6951, 1077-3118. DOI: 10.1063/1.1343846.

[25] L. Farrell et al. "Conducting mechanism in the epitaxial *p*-type transparent conducting oxide Cr_2O_3:Mg". In: *Physical Review B* 91.12 (2015), p. 125202. ISSN: 1098-0121, 1550-235X. DOI: 10.1103/PhysRevB.91.125202.

[26] E. Arca, K. Fleischer, and I. V. Shvets. "Magnesium, nitrogen codoped Cr_2O_3: A *p*-type transparent conducting oxide". In: *Applied Physics Letters* 99.11 (2011), p. 111910. ISSN: 0003-6951. DOI: 10.1063/1.3638461.

[27] Alexander Polyakov et al. "Electrical properties of α-Ga2O3 films grown by halide vapor phase epitaxy on sapphire with α-Cr2O3 buffers". In: *Journal of Applied Physics* 131.21 (2022), p. 215701. ISSN: 0021-8979, 1089-7550. DOI: 10.1063/5.0090832.

[28] Alexander Polyakov et al. "Effects of sapphire substrate orientation on Sn-doped α-Ga_2O_3 grown by halide vapor phase epitaxy using α-Cr_2O_3 buffers". In: *Journal of Physics D: Applied Physics* 55.49 (2022), p. 495102. ISSN: 0022-3727, 1361-6463. DOI: 10.1088/1361-6463/ac962f.

[29] Anna Caricato et al. "Deposition of chromium oxide thin films with large thermoelectromotive force coefficient by reactive pulsed laser ablation". In: *Journal of Optoelectronics and Advanced Materials* 12 (2010), p. 427.

[30] Sandhyarani Punugupati, Jagdish Narayan, and Frank Hunte. "Room temperature ferromagnetism in epitaxial Cr_2O_3 thin films grown on r-sapphire". In: *Journal of Applied Physics* 117.19 (2015), p. 193907. ISSN: 0021-8979, 1089-7550. DOI: 10.1063/1.4921435.

[31] Elisabetta Arca et al. "Valence band modification of Cr_2O_3 by Ni-doping: creating a high figure of merit *p*-type TCO". In: *Journal of Materials Chemistry C* 5.47 (2017), pp. 12610–12618. ISSN: 2050-7534. DOI: 10.1039/C7TC03545D.

[32] P. Kofstad and K. P. Lillerud. "On High Temperature Oxidation of Chromium: II . Properties of and the Oxidation Mechanism of Chromium". In: *Journal of The Electrochemical Society* 127.11 (1980), pp. 2410–2419. ISSN: 0013-4651, 1945-7111. DOI: 10.1149/1.2129481.

[33] A Holt and P Kofstad. "Electrical conductivity and defect structure of Cr_2O_3. II. Reduced temperatures (<∼1000 °C)". In: *Solid State Ionics* 69.2 (1994), pp. 137–143. ISSN: 01672738. DOI: 10.1016/0167-2738(94)90402-2.

[34] Robert Schewski et al. "Epitaxial stabilization of pseudomorphic α-Ga_2O_3 on sapphire (0001)". In: *Applied Physics Express* 8.1 (2015), p. 011101. ISSN: 1882-0778, 1882-0786. DOI: 10.7567/APEX.8.011101.

[35] Kentaro Kaneko et al. "Progress in α-Ga_2O_3 for practical device applications". In: *Japanese Journal of Applied Physics* 62 (SF 2023), SF0803. ISSN: 0021-4922, 1347-4065. DOI: 10.35848/1347-4065/acd125.

[36] S. J. Pearton et al. "A review of Ga_2O_3 materials, processing, and devices". In: *Applied Physics Reviews* 5.1 (2018), p. 011301. ISSN: 1931-9401. DOI: 10.1063/1.5006941.

[37] Duyoung Yang et al. "Epitaxial growth of alpha gallium oxide thin films on sapphire substrates for electronic and optoelectronic devices: progress and perspective". In: *Electronic Materials Letters* 18.2 (2022), pp. 113–128. ISSN: 1738-8090, 2093-6788. DOI: 10.1007/s13391-021-00333-5.

[38] Kentaro Kaneko et al. "Evaluation of misfit relaxation in α-Ga_2O_3 epitaxial growth on α-Al_2O_3 substrate". In: *Japanese Journal of Applied Physics* 51 (2R 2012), p. 020201. ISSN: 0021-4922, 1347-4065. DOI: 10.1143/JJAP.51.020201.

[39] Riena Jinno et al. "Reduction in edge dislocation density in corundum-structured α-Ga_2O_3 layers on sapphire substrates with quasi-graded α-$(Al,Ga)_2O_3$ buffer layers". In: *Applied Physics Express* 9.7 (2016), p. 071101. ISSN: 1882-0778, 1882-0786. DOI: 10.7567/APEX.9.071101.

[40] Riena Jinno et al. "Crystal orientation dictated epitaxy of ultrawide-bandgap 5.4- to 8.6-eV α-$(AlGa)_2O_3$ on m-plane sapphire". In: *Science Advances* 7.2 (2021), eabd5891. ISSN: 2375-2548. DOI: 10.1126/sciadv.abd5891.

[41] Anna Hassa et al. "Control of phase formation of $(Al_xGa_{1-x})_2O_3$ thin films on c-plane Al_2O_3". In: *Journal of Physics D: Applied Physics* 53.48 (2020), p. 485105. ISSN: 0022-3727, 1361-6463. DOI: 10.1088/1361-6463/abaf7d.

[42] L. D. Landau and E. M. Lifshitz. *Theory of Elasticity*. Course of Theoretical Physics vol. 7. Pergamon Press Ltd., 1970. 165 pp. ISBN: 978-0-08-057069-3.

[43] Marius Grundmann. "Elastic theory of pseudomorphic monoclinic and rhombohedral heterostructures". In: *Journal of Applied Physics* 124.18 (2018), p. 185302. ISSN: 0021-8979, 1089-7550. DOI: 10.1063/1.5045845.

[44] H.L. Alberts and J.C.A. Boeyens. "The elastic constants and distance dependence of the magnetic interactions of Cr_2O_3". In: *Journal of Magnetism and Magnetic Materials* 2.4 (1976), pp. 327–333. ISSN: 03048853. DOI: 10.1016/0304-8853(76)90044-5.

[45] Marius Grundmann. "A most general and facile recipe for the calculation of heteroepitaxial strain". In: *physica status solidi (b)* 257.12 (2020), p. 2000323. ISSN: 0370-1972, 1521-3951. DOI: 10.1002/pssb.202000323.

[46] Max Kneiß et al. "Strain states and relaxation for α-$(Al_xGa_{1-x})_2O_3$ thin films on prismatic planes of α-Al_2O_3 in the full composition range: Fundamental difference of a- and m-epitaxial planes in the manifestation of shear strain and lattice tilt". In: *Journal of Materials Research* 36.23 (2021), pp. 4816–4831. ISSN: 0884-2914, 2044-5326. DOI: 10.1557/s43578-021-00375-3.

[47] Marius Grundmann. *The Physics of Semiconductors: An Introduction Including Nanophysics and Applications*. Graduate Texts in Physics. Cham: Springer International Publishing, 2016. ISBN: 978-3-319-23879-1 978-3-319-23880-7. URL: http://link.springer.com/10.1007/978-3-319-23880-7.

[48] Derek Hull and D. J. Bacon. *Introduction to Dislocations*. 5th ed. Elsevier Ltd., 2011. 268 pp. ISBN: 978-0-08-096673-1.

[49] M. Grundmann and M. Lorenz. "Anisotropic strain relaxation through prismatic and basal slip in α-(Al, Ga)$_2$O$_3$ on R-plane Al_2O_3". In: *APL Materials* 8.2 (2020), p. 021108. ISSN: 2166-532X. DOI: 10.1063/1.5144744.

[50] M. Grundmann, T. Stralka, and M. Lorenz. "Epitaxial growth and strain relaxation of corundum-phase (Al,Ga)$_2$O$_3$ thin films from pulsed laser deposition at 1000 °C on r-plane Al_2O_3". In: *Applied Physics Letters* 117.24 (2020), p. 242102. ISSN: 0003-6951, 1077-3118. DOI: 10.1063/5.0030675.

[51] Michael Lorenz. "Pulsed laser deposition". In: *Encyclopedia of Applied Physics*. Wiley, 2019. URL: http://dx.doi.org/10.1002/3527600434.eap810.

[52] Holger von Wenckstern et al. "A review of the segmented-target approach to combinatorial material synthesis by pulsed-laser deposition". In: *Phy. Status Solidi B* 257.7 (2020), p. 1900626. ISSN: 0370-1972, 1521-3951. DOI: 10.1002/pssb.201900626.

[53] V. Srikant, J. S. Speck, and D. R. Clarke. "Mosaic structure in epitaxial thin films having large lattice mismatch". In: *Journal of Applied Physics* 82.9 (1997), pp. 4286–4295. ISSN: 0021-8979, 1089-7550. DOI: 10.1063/1.366235.

[54] Sofie Vogt et al. "Realization of Conductive n-Type Doped α-Ga_2O_3 on *m*-Plane Sapphire Grown by a Two-Step Pulsed Laser Deposition Process". In: *physica status solidi (a)* 220.3 (2023), p. 2200721. ISSN: 1862-6300, 1862-6319. DOI: 10.1002/pssa.202200721.

[55] L. J. van der Pauw. "A method of measuring specific resistivity and Hall effect of discs of arbitrary shape". In: *Philips Research Reports* 13.1 (1958), pp. 1–9.

[56] Hiroyuki Fujiwara. *Spectroscopic Ellipsometry. Principles and Applications*. Tōkyō: John Wiley & Sons, Ltd, 2007. ISBN: 978-4-621-07253-0.